

## Article

# Characterisation of Harmonic Resonance Phenomenon of Multi-Parallel PV Inverter Systems: Modelling and Analysis

Kasun Peiris , Sean Elphick , Jason David  and Duane Robinson \* 

Australian Power Quality Research Centre, University of Wollongong, Wollongong, NSW 2522, Australia; mkdp331@uowmail.edu.au (K.P.); elpho@uow.edu.au (S.E.); jd660@uowmail.edu.au (J.D.)

\* Correspondence: duane@uow.edu.au

**Abstract:** Solar PV inverters require output filters to reduce unwanted harmonics in their output, where LCL filters are a more economical choice than larger inductance-only filters. A drawback of these filters is that they can introduce power quality disturbances, especially at higher frequencies (above 2 kHz). This paper investigates and characterises the resonance phenomenon introduced by different filter types, i.e., LC or LCL, and identifies their behavioural change when combined with multiple parallel grid-tied PV inverter systems. MATLAB/Simulink modelling aspects of PV inverter systems related to resonance phenomenon are presented, including establishing resonance at a specific frequency where potentially large variations in the parameter selection across manufacturers may exist. In addition, a method is developed to establish output filter frequency response through measurements, which is used to develop validated solar PV harmonic models for high-frequency analysis. The low-frequency harmonic models can be used up to the resonant frequency where the current flowing through the filter capacitor is insignificant compared to the current flowing into the electricity network.

**Keywords:** resonance; frequency response; MATLAB/Simulink modelling; supraharmonics; solar PV inverter



Academic Editor: Wajiha Shireen

Received: 3 December 2024

Revised: 10 January 2025

Accepted: 16 January 2025

Published: 20 January 2025

**Citation:** Peiris, K.; Elphick, S.; David, J.; Robinson, D. Characterisation of Harmonic Resonance Phenomenon of Multi-Parallel PV Inverter Systems: Modelling and Analysis. *Energies* **2025**, *18*, 443. <https://doi.org/10.3390/en18020443>

**Copyright:** © 2025 by the authors. Licensee MDPI, Basel, Switzerland. This article is an open access article distributed under the terms and conditions of the Creative Commons Attribution (CC BY) license (<https://creativecommons.org/licenses/by/4.0/>).

## 1. Introduction

Solar PV generation has become one of the most promising renewable energy sources to be deployed, where its capacity additions range from industrial MW-scale down to household kW-scale installations [1]. Solar PV inverters require output passive filters, i.e., LC or LCL configurations, to suppress the magnitude of harmonic emissions injected into the electricity supply network [2]. However, power quality disturbances may increase with these filters due to the introduction of resonance phenomena at a specific frequency. The analysis of the resonance phenomenon associated with solar PV inverters is not a new topic, and methods to suppress the impact of resonance have been studied extensively [3–5]. LCL filters are generally a more economical choice for inverter manufacturers in terms of performance, with the design of LCL filters already investigated in [6–8]. Filter resonance damping can be achieved by adding a resistor to the filter network, which leads to additional power loss in the filter.

With the advancements in power electronics, PV inverters use switching frequencies in the 2–20 kHz range, which reduces harmonic emissions in the lower-frequency range (<2 kHz). However, it has increased high-frequency emissions, also referred to as ‘supraharmonics’ [9]. The shifting of resonance phenomenon above 2 kHz can introduce system disturbances at higher frequencies, which may be critical for network operators.

There are several control techniques have been developed to increase the system stability and control performance, and suppress the grid current harmonics. Investigation of six passive damping solutions based on the location of the resistor is provided in [10]. In [11], a full feed-forward harmonic suppression scheme is presented by adding a virtual admittance to the system through modifications in the inverter control loop, which cancels out the output equivalent admittance. A capacitive current feedback active damping strategy is presented in [12] that can be utilised in weak grid conditions. In addition, different *LCL* filter parameter calculations were presented in [13,14]. However, all those techniques have been considered for a single-inverter operation only. The understanding of resonance characteristics for a multiple inverter system based on both individual inverter terminal currents and the summated current has not been widely investigated.

The modelling of solar PV inverters for high-frequency harmonic analysis is an emerging area and limitations exist to incorporating low-frequency (<2 kHz) models for high-frequency (>2 kHz) analysis [15]. Different modelling techniques have been investigated for high-frequency analysis: frequency domain analysis for transient analysis [16]; black box modelling over white box modelling [17]; and measurement-based modelling [18]. Yet a suitably accurate generic solar PV model to analyse high-frequency harmonics has not been developed. The modelling of solar PV inverters is important to fully understand the supraharmonic behaviour despite the complete in-detail model only being available to the inverter manufacturer [15]. The complex filter design criteria used by inverter manufacturers and large variations in filter component value calculations make it difficult to assess the accuracy of filter design based on measurements alone.

This paper provides insights into filter component selection in order to obtain the resonance phenomena at a specific frequency. In this study, responses of three different filter types, i.e., *LCL*, *LC* and common core reactor, are characterised based on: (a) forward self-admittance; (b) forward trans-admittance; and (c) ratio between grid-side current and inverter-side current. Supporting the work presented in [19], derived transfer functions for a multiple inverter system where resonant characteristics were identified for both individual inverter terminal currents and the aggregation currents. A MATLAB/Simulink model is developed and validated emphasizing the modelling aspects of resonance phenomenon. The model is used to understand the impact of grid stiffness as multiple resonant points can be identified for a weaker grid condition.

The reversed engineering technique of filter design can be useful to validate high-frequency models with on-site or laboratory measurements. This work is part of a larger piece attempting to understand higher frequency harmonic levels and propagation associated with solar PV inverters.

### *Organization of the Paper*

The aims of this paper are to identify resonance characteristics of a solar PV inverter system and provide harmonic modelling aspects to establish output filter frequency response aligning with measurements. Section 2 provides characteristics of a passive *LCL* filter based on transfer functions derived. Thévenin equivalent model is used for analysis. Section 3 provides an extension to Section 2 considering the instance of multiple PV inverter systems to further characterise resonance. The impact of both *LC* and *LCL* filter types when the number of inverters increases is discussed. Section 4 provides on-site measurements of a solar PV system with six identical inverters to identify the resonance phenomenon. The modelling aspects to obtain resonance at a specific frequency are given in Section 5. Section 6 provides the resonance characteristics based on a generic MATLAB/Simulink model developed for a multiple PV inverter system. Section 7 provides the analysis between measurements and simulation results with the developed model. In addition to

the conventional filters, a common core choke is included within the modelling. Section 8 presents the critical analysis of resonance characteristics of a multiple inverter systems. It is demonstrated that the peak magnitude and the frequency of the resonance changes with a number of energised inverters.

## 2. LCL Filter Overview

This section provides a theoretical background of *LCL* filter characteristics to better understand the different filter design approaches incorporated in the literature. The *LCL* filter is generally used to attenuate high-frequency harmonics, especially switching ripples generated by high-frequency PWM signals. Unlike the *L* filter, small increases in inductor values of an *LCL* filter can attenuate the switching ripples significantly [20]. The detailed equivalent models of a passive *LCL* filter and the control block diagram are shown in Figure 1, where the components can be characterised as follows.

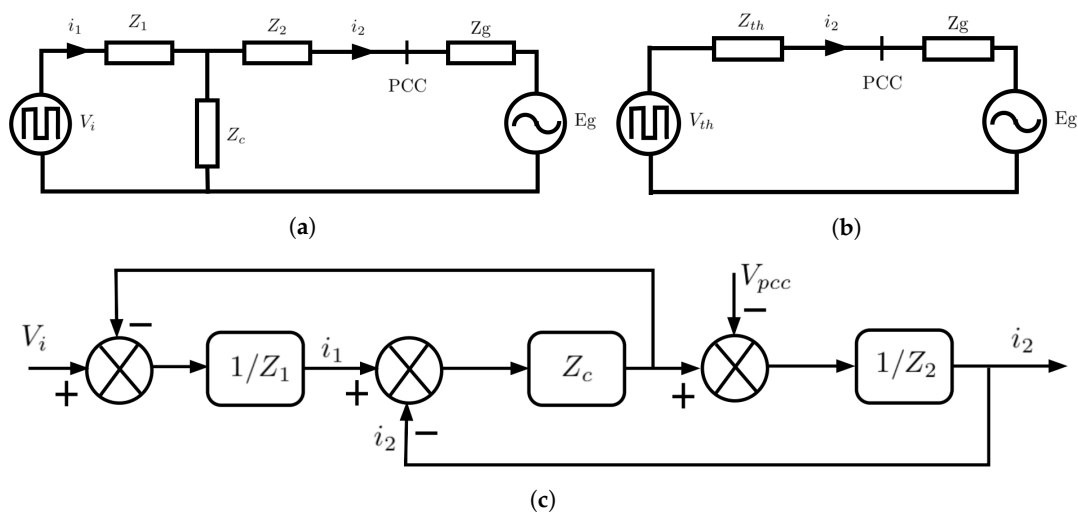


**Figure 1.** Passive *LCL* filter: (a) general arrangement; (b) Thévenin equivalent; and (c) control block diagram.

$$\begin{aligned}
 Z_1 &= R_1 + L_1s \\
 Z_2 &= R_2 + L_2s \\
 Z_c &= R_d + \frac{1}{C_f s} \\
 Z_g &= R_g + L_g s
 \end{aligned} \tag{1}$$

where  $Z_1$ ,  $Z_2$ ,  $Z_c$  and  $Z_g$  are the equivalent inverter-side, grid-side, capacitor branch and grid impedances, respectively;  $L_1$  and  $R_1$  are the inverter-side inductor and equivalent series resistor;  $L_2$  and  $R_2$  are the grid-side inductor and equivalent series resistor;  $C_f$  and  $R_d$  are the capacitance of the *LCL* filter and the series damping resistor;  $L_g$  and  $R_g$  are the grid inductor and resistor;  $V_i$  and  $E_g$  are the filter input voltage and Thévenin equivalent grid voltage;  $V_{th}$  and  $Z_{th}$  are the Thévenin equivalent voltage and impedance of *LCL* filter, respectively, as expressed in the following equations.

$$\begin{aligned}
 V_{th} &= V_i \left[ \frac{Z_c}{Z_1 + Z_c} \right] \\
 k_{th} &= \left[ \frac{Z_c}{Z_1 + Z_c} \right] \\
 V_{th} &= k_{th} \cdot V_i
 \end{aligned} \tag{2}$$

$$\begin{aligned} Z_{th} &= Z_2 + Z_1 // Z_c \\ Z_{th} &= \left[ \frac{Z_2 Z_1 + Z_2 Z_c + Z_1 Z_c}{Z_1 + Z_c} \right] \end{aligned} \quad (3)$$

The current flowing through the  $Z_2$  impedance is the same as the current flowing through  $Z_{th}$  impedance. Therefore, the  $i_2$  can be calculated according to (4).

$$i_2 = \frac{V_{th}}{Z_{th} + Z_g} \quad (4)$$

By substituting  $V_{th}$  into (4) the current through the grid-side inductor in the frequency domain can be re-written as follows.

$$i_2(s) = \frac{k_{th}}{Z_{th} + Z_g} \cdot V_i(s) \quad (5)$$

There are three main transfer functions used to determine *LCL* filter performance. These transfer functions are helpful in determining filter parameters and to use with the current control of the inverter, which can be written as follows:

$$\begin{aligned} G_1 &= \frac{i_1(s)}{V_i(s)} = \frac{Z_c + Z_2 + Z_g}{Z_1(Z_2 + Z_g) + Z_1 Z_c + Z_c(Z_2 + Z_g)} \\ G_2 &= \frac{i_2(s)}{V_i(s)} = \frac{Z_c}{Z_1(Z_2 + Z_g) + Z_1 Z_c + Z_c(Z_2 + Z_g)} \\ G_3 &= \frac{i_2(s)}{i_i(s)} = \frac{Z_c}{Z_c + Z_2 + Z_g} \end{aligned} \quad (6)$$

where  $G_1$  and  $G_2$  represent the forward self-admittance and the forward trans-admittance, respectively;  $G_3$  represents the attenuation between the grid-side current and inverter-side current.

The parasitic resistances of the components account for the damping effect. In the worst-case scenario, these parasitic resistance values are neglected; thus, the above transfer functions can be rearranged as follows.

$$\begin{aligned} G_1 &= \frac{i_1(s)}{V_i(s)} = \frac{1 + C_f(L_2 + L_g)s^2}{L_1 C_f(L_2 + L_g)s^3 + (L_1 + L_2 + L_g)s} \\ G_2 &= \frac{i_2(s)}{V_i(s)} = \frac{1}{L_1 C_f(L_2 + L_g)s^3 + (L_1 + L_2 + L_g)s} \\ G_3 &= \frac{i_2(s)}{i_i(s)} = \frac{1}{1 + C_f(L_2 + L_g)s^2} \end{aligned} \quad (7)$$

Bode plots of  $G_1$ ,  $G_2$ , and  $G_3$  are presented in Figure 2, where two resonant frequencies can be identified for  $G_1$ . The common denominator of  $G_1$  and  $G_2$  resulting in a common resonant frequency ( $\omega_{res,1}$ ) at the frequency given by (8). In addition, a dip can be identified in  $G_1$  at  $\omega_{res,2}$  which is given in (9).

$$\omega_{res,1} = \sqrt{\frac{L_1 + (L_2 + L_g)}{L_1(L_2 + L_g)C_f}} \quad (8)$$

$$\omega_{res,2} = \sqrt{\frac{1}{(L_2 + L_g)C_f}} \quad (9)$$

The damping resistor ( $R_d$ ) placed in series with the filter capacitor has a major influence on the magnitude of the resonance peak as shown in Figure 2b. A small damping

resistance may greatly dampen the resonance peak improving the system stability; however, the filter losses may increase, which must be considered when designing the filter. The introduction of the damping resistor affects the transfer functions depicted in (7) whereby the forward trans-admittance is changed to

$$G_2 = \frac{i_2(s)}{V_i(s)} = \frac{1 + C_f R_d s}{[L_1(L_2 + L_g)C_f]s^3 + [L_1(L_2 + L_g)C_f R_d]s^2 + (L_1 + L_2 + L_g)s} \quad (10)$$

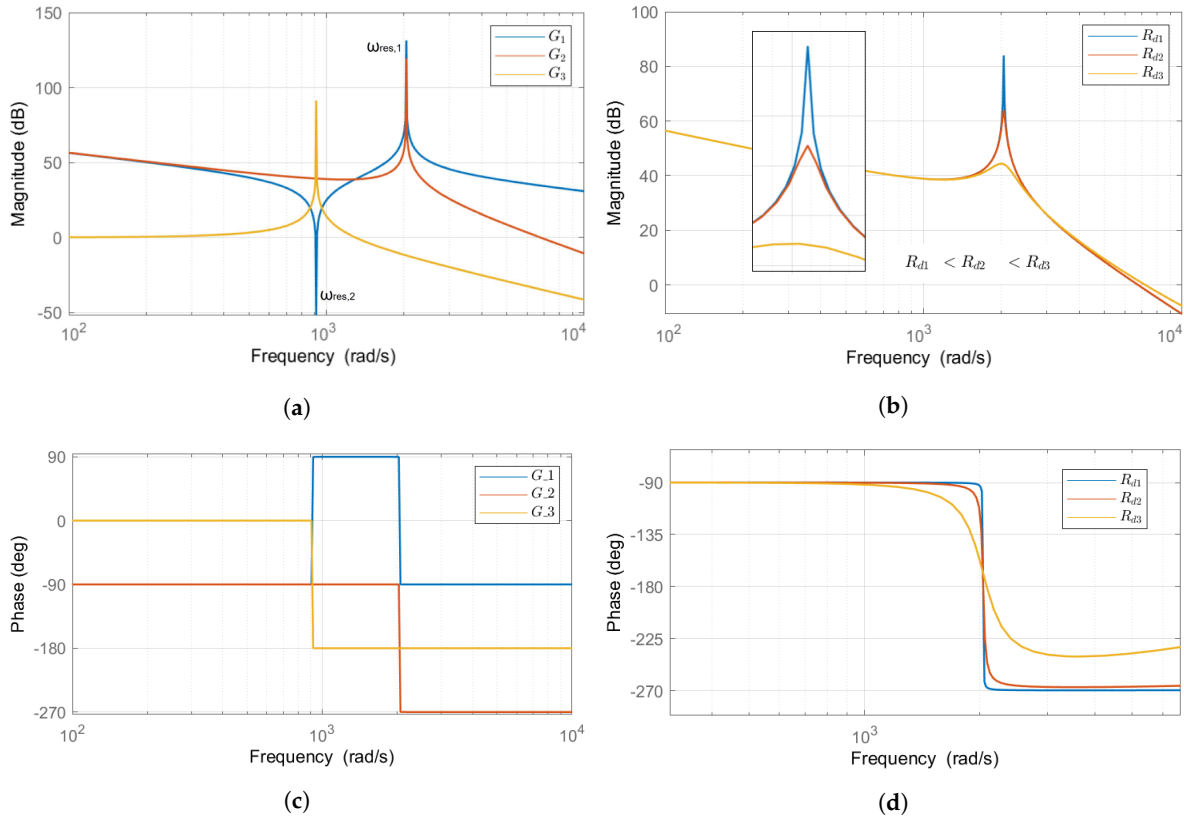


**Figure 2.** Transfer functions plot and damping resistor impact on resonance: (a) magnitude plot of  $G_1$ ,  $G_2$ , and  $G_3$ ; (b) impact of damping resistor on resonance peak of  $G_2$ ; (c) phase angle plot of  $G_1$ ,  $G_2$ , and  $G_3$ ; and (d) damping resistor impact on phase angles of  $G_2$ .

The magnitude plot of each transfer function is depicted in Figure 3 to understand its behaviour at lower frequencies and higher frequencies. As seen in Figure 3a, below the resonant frequency, the filter can be approximated by the sum of all inductor values ( $L_1 + L_2 + L_g$ ), and above the resonant frequency, the filter can be approximated by the grid-side inductance alone ( $L_1$ ). It can be concluded that, at higher frequencies, above resonant frequency, the capacitor branch acts as a short circuit path as seen from the inverter side.

Similarly, Figure 3b indicates that below the resonant frequency, the filter can be approximated by the sum of all inductor values ( $L_1 + L_2 + L_g$ ). Unlike self-admittance characteristics, trans-admittance magnitudes attenuate rapidly after  $\omega_{res,2}$ . The same characteristics can be identified in Figure 3c, where up to  $\omega_{res,2}$  inverter-side current ( $i_1$ ) almost equals the grid-side current ( $i_2$ ), approximating no impact by the capacitor. Beyond this frequency, a large portion of the inverter-side current flows through the capacitor creating a dominant circulating current within the inverter.

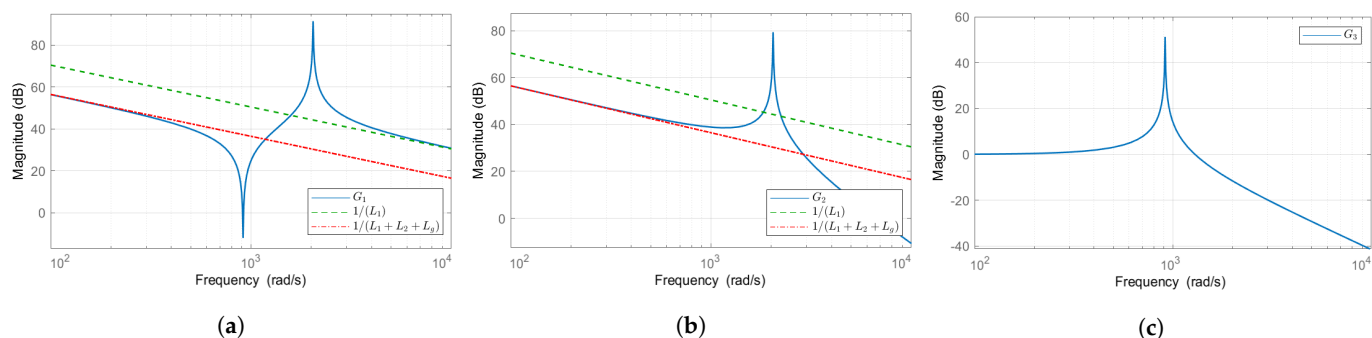


**Figure 3.** Magnitude Bode Plot of: (a)  $G_1$ ; (b)  $G_2$ ; and (c)  $G_3$ .

Developing harmonic models is a challenging task, as the low-frequency models may not be valid for high-frequency analysis. Determination of the impact of the front-end filter is essential to overcome this issue, as at high frequencies, the circulating current component is dominant. However, it can be estimated that up to the resonant frequency given by  $\omega_{res,2}$ , low-frequency harmonics models can be extended as there is minimal circulation current impact.

There is a clear and concise explanation of the filter design process in [10,21]. It highlights the importance of verifying component values against two key constraints: resonant frequency; and inductor voltage drop. This iterative approach ensures that the filter meets the desired specifications. The process for filter design is presented in Appendix A, where calculation of  $LCL$  values is much easier using the mentioned steps and the filter designer has the freedom to decide the resonant frequency placement.

According to the literature, there is a large variation in the parameter selection of design of the  $LCL$  filter, as summarised in Table 1.

**Table 1.**  $LCL$  filter values calculation by the literature.

Ref.	Max. Ripple Current (Converter-Side Inductance)	Attenuation Rate (Grid-Side Inductance)	Filter Capacitance	Remarks
[20]	$(15\text{--}35\%) \cdot i_{rated}$		$15\% \cdot C_{base}$	Ripple current: 33.5% of rated current, capacitor: 15% of the base capacitance
[22]	$(20\text{--}40\%) \cdot i_{rated}$	10%	$(2\text{--}5\%) \cdot C_{base}$	Ripple current: 40% of rated current, capacitor: 2% of the base capacitance
[23,24]	$10\% \cdot i_{rated}$	60%	$5\% \cdot C_{base}$	$L_1$ calculation is different. Divided by 6 instead of 8
[25]	$5\% \cdot i_{rated}$	20%	$5\% \cdot C_{base}$	Single phase rectifier, $L_1$ calculation is different. Divided by 4 instead of 8
[26]	$20\% \cdot i_{rated}$		$5\% \cdot C_{base}$	$L_2$ calculated based on the maximum allowed voltage drop
[27]	5 mH	2 mH	2 $\mu$ F	Maximum allowed ripple current: 4 A. $f_{sw} = 10$ kHz, $P = 4$ kW, $V_{dc} = 600$ V

### 3. Resonance Introduced by Multi-Parallel Inverter System

This section provides theoretical background resonance phenomenon due to a multi-parallel grid-tied inverter system, extending the work presented in Section 2. The parallel operation of multiple PV inverters also introduces a resonance phenomenon [19,28,29]. A system with  $n$  identical inverters in parallel is presented in Figure 4. Inverter output current (current flows through  $L_2$  inductor) is denoted by  $i_{2,x}$ , where  $x$  represents the

inverter number. Similarly, equivalent Thévenin voltage and impedance are denoted with the same suffix to mention the inverter number.

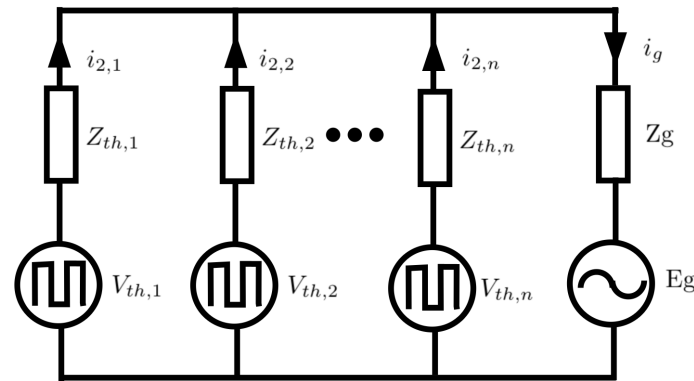


Figure 4.  $n$  identical inverters are connected in parallel.

Analysis of the system reveals that each inverter grid-side current  $i_{2,x}$ , i.e.,  $x = 1$ , is influenced by two parts. The first part is the influence caused by its own inverter voltage output  $V_{i,x}$ , i.e.,  $x = 1$ . The second part is the influence caused by all other inverter voltages, i.e.,  $x = 2, 3, \dots, n$ , on the selected inverter grid-side current, which is due to the coupling effect between inverters. Contrary to single-inverter operation, additional inverters influence the current flowing through every inverter.

$$i_2 = G_2 \times V_i$$

$$\begin{bmatrix} i_{2,1} \\ i_{2,2} \\ \vdots \\ i_{2,n} \end{bmatrix} = \begin{bmatrix} G_{2,11} & G_{2,12} & \cdots & G_{2,1n} \\ G_{2,21} & G_{2,22} & \cdots & G_{2,2n} \\ \vdots & \vdots & \ddots & \vdots \\ G_{2,n1} & G_{2,n2} & \cdots & G_{2,nn} \end{bmatrix} \times \begin{bmatrix} V_{i,1} \\ V_{i,2} \\ \vdots \\ V_{i,n} \end{bmatrix} \quad (11)$$

$G_2$  consists of  $n \times n$  matrix where diagonal elements indicate the impact of self-inverter voltage, which results in identical diagonal values for identical PV inverter systems. Similarly, off-diagonal elements are the same and indicate the impact of other inverters of the system. The diagonal elements are given by  $G_{2,xx}$  and off-diagonal elements are given by  $G_{2,xy}$ . The grid current component of each inverter  $G_{2,gx}$  is derived to identify the characteristics of the grid-current component. The equations for  $Z_M$  and transfer functions are modified as follows:

$$Z_M = \left[ \frac{Z_{th}Z_g}{Z_{th} + (n-1)Z_g} \right]$$

$$G_{2,xx} = \frac{k_{th}}{Z_{th} + Z_M} \quad (12)$$

$$G_{2,xy} = \left[ \frac{Z_g}{(n-1)Z_g + Z_{th}} \right] \cdot \left[ \frac{k_{th}}{Z_{th} + Z_M} \right]$$

$$G_{2,gx} = G_{2,xx} - (n-1)G_{2,xy}$$

For a two-inverter system, derivation of (12) is explained and provided in Appendix B.

### 3.1. LCL Filters

For a single inverter with front-end LCL filters, Thévenin equivalent voltage ( $V_{th}$ ) and Thévenin equivalent impedance ( $Z_{th}$ ) are given by (2) and (3), respectively. The frequency response for the characteristics derived in (12) is depicted in Figure 5 to identify the resonance characteristics of a multiple inverter system with LCL filters.

The selection of filter components is discussed in detail in Section 5 according to the system parameters given in Table 2. The filter values used to derive in Figure 5 plots are similar to the values given in Table 3.

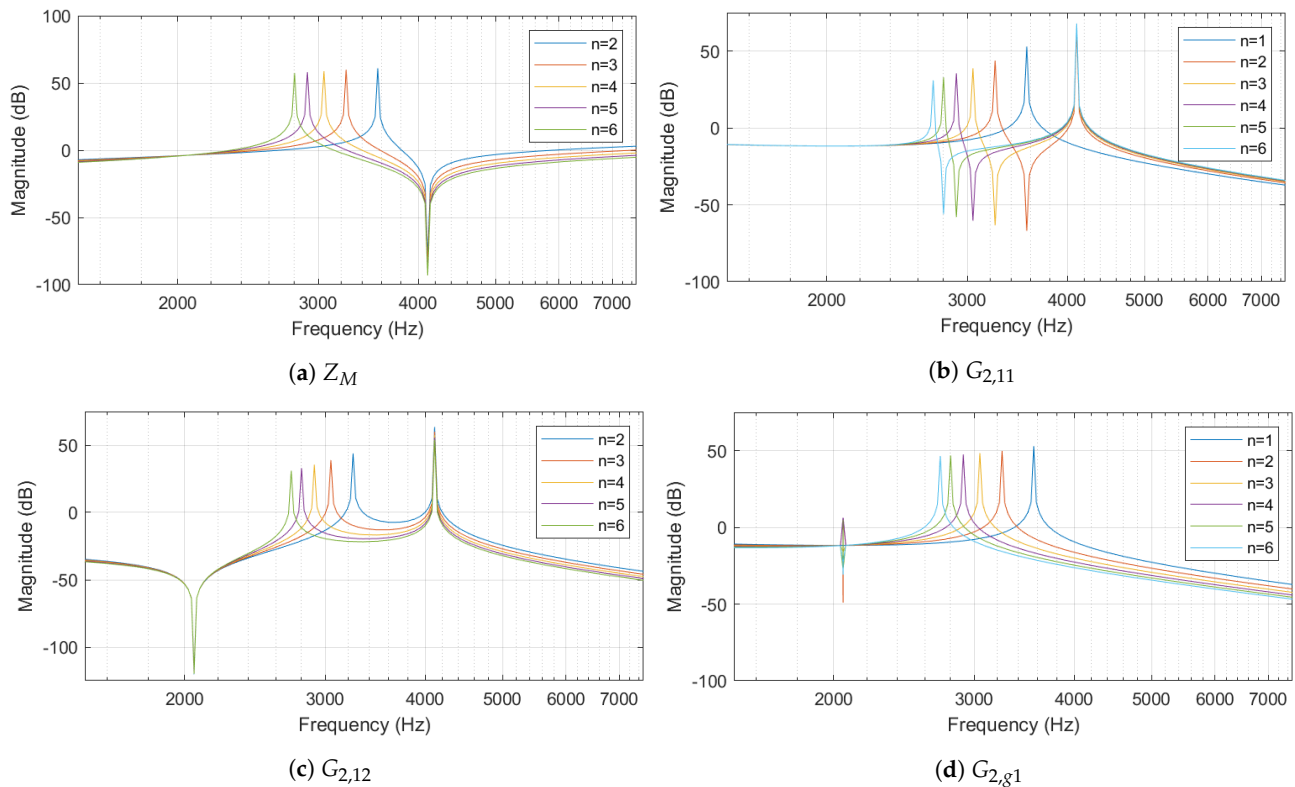


**Figure 5.** Frequency characteristics of *LCL* filter: (a) grid impedance seen by an individual inverter; (b)  $G_{2,11}$  transfer function; (c)  $G_{2,12}$  transfer function; and (d)  $G_{2,g1}$  transfer function.

The findings related to the characteristics of the *LCL* filter resonance phenomenon are as follows:

- The equivalent impedance seen by an individual inverter ( $Z_M$ ) is depicted in Figure 5a. For single-inverter operation ( $n = 1$ ),  $Z_M$  equals to  $Z_g$ , which is directly proportional to the frequency. However, for a given  $n$  ( $n > 1$ ), maximum and minimum impedance points can be identified.
- The frequency response of  $G_{2,11}$  is depicted in Figure 5b, which represents the diagonal elements of the  $G_2$ . When  $n = 1$ , there is only one resonance point where the resonant frequency is given by  $f_{res,1}$ . When additional inverters connect, two resonances can be seen where resonant frequencies are given in (13). The peak magnitude of the resonance decreases as the number of inverters ( $n$ ) increases. In addition to the two peaks, a dip can also be identified, which corresponds to the maximum impedance seen by the inverter in Figure 5a.

$$f_{LCL} = \frac{1}{2\pi} \sqrt{\frac{L_1 + L_2}{L_1 \cdot L_2 \cdot C_f}} \quad (13)$$

$$f_{res,n} = \frac{1}{2\pi} \sqrt{\frac{L_1 + L_2 + (n-1)L_g}{L_1 \cdot [L_2 + (n-1)L_g] \cdot C_f}}$$

- The frequency response of  $G_{2,21}$  is depicted in Figure 5c, which represents the off-diagonal elements of the  $G_2$ . The frequencies corresponding to the magnitude peaks are similar to those given by (13).

- The frequency response of  $G_{2,g1}$  is depicted in Figure 5d, which represents the grid current component of an inverter. Assuming identical inverters, this does not change the total grid current summed up for each inverter. Only one resonance peak can be identified. When the number of inverters increases, the resonant frequency decreases and the magnitude of the resonance peak is damped.
- The frequency spectrum from an individual inverter terminal current does not tally with the frequency spectrum of grid current (summation of each inverter current) according to Figure 5b,d when  $n > 1$ . Two resonant frequencies for the individual inverter terminal and only one resonant frequency for the grid current.

### 3.2. LC Filters

For inverters with front-end LC filters, the Thévenin equivalent voltage ( $V_{th}$ ) and Thévenin equivalent impedance ( $Z_{th}$ ) are to be modified by approximating grid-side inductance of the LCL filter to be zero as in (14). Substituting (14) into (12), the new parameters for the LC filter are calculated. The same filter component values as in the LCL filter were used to identify the characteristics of the LC filter resonance. The only difference is the absence of the  $L_2$  inductor. The frequency response is depicted in Figure 6 to identify the resonance characteristics of a multiple inverter system with LC filters.

$$Z_{th} = Z_1 // Z_c$$

$$Z_{th} = \left[ \frac{Z_1 Z_c}{Z_1 + Z_c} \right] \tag{14}$$

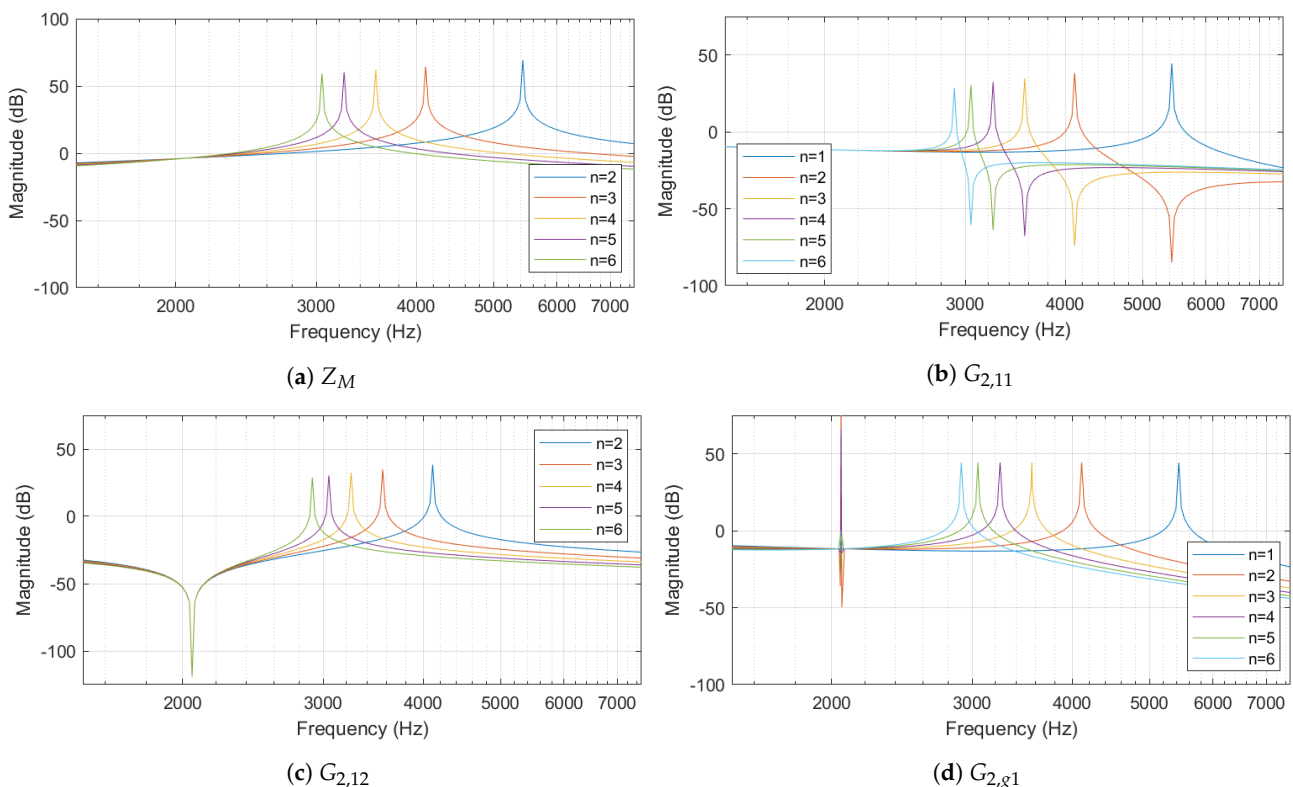


**Figure 6.** Frequency characteristics of LC filter: (a) grid impedance seen by an individual inverter; (b)  $G_{2,11}$  transfer function; (c)  $G_{2,12}$  transfer function; and (d)  $G_{2,g1}$  transfer function.

The findings related to the characteristics of LC filter resonance are as follows:

- The equivalent impedance seen by an individual inverter ( $Z_M$ ) seen by an individual inverter is depicted in Figure 6a. Similar to the LCL filter, for a single-inverter opera-

tion ( $n = 1$ ),  $Z_M$  equals  $Z_g$ , which is directly proportional to the frequency. However, for a given  $n$  ( $n > 1$ ), unlike  $LCL$  filters, only one impedance peak is identified.

- The frequency response of  $G_{2,11}$  is depicted in Figure 6b, which represents the diagonal elements of the  $G_2$ . Only one resonance point can be seen where resonant frequencies are calculated using (15). The resonance peak decreases as  $n$  increases. In addition to the peak, a dip can also be identified, which corresponds to the maximum impedance seen by the inverter in Figure 6a.

$$f_{res,n} = \frac{1}{2\pi} \sqrt{\frac{L_1 + nL_g}{L_1 \cdot n \cdot L_g \cdot C_f}} \quad (15)$$

- The frequency response of  $G_{2,g1}$  is depicted in Figure 6d, which represents the grid current component of an inverter. Only one resonance peak can be identified. With the number of inverters increasing, the resonant frequency decreases and the resonance peak is damped.
- The frequency spectrum of an individual inverter terminal current, tally with the frequency spectrum of the grid current (summation of each inverter current) according to Figure 6b,d.

#### 4. Identifying Resonance Phenomenon with Field Measurements

This section provides the on-site measurements to identify the resonance phenomenon associated with solar PV inverters. Theoretical analysis carried out in Section 3 considering only the passive filter components. The advanced controlling techniques implemented by inverter manufacturers have not been considered. A multiple PV inverter system with six identical 20 kW inverters (labelled A–F) was monitored to identify the resonance phenomenon with measurements. The total power output is fed into the grid through two separate circuits. A Hioki MR8847A Memory HiCorder device recorded individual inverter current waveforms and the combined current with high-frequency current clamps. Due to the limitation of the device, only four channels, one phase from inverters A, B, and C, and one circuit of the aggregation circuit were measured. The measurement setup is illustrated in Figure 7.

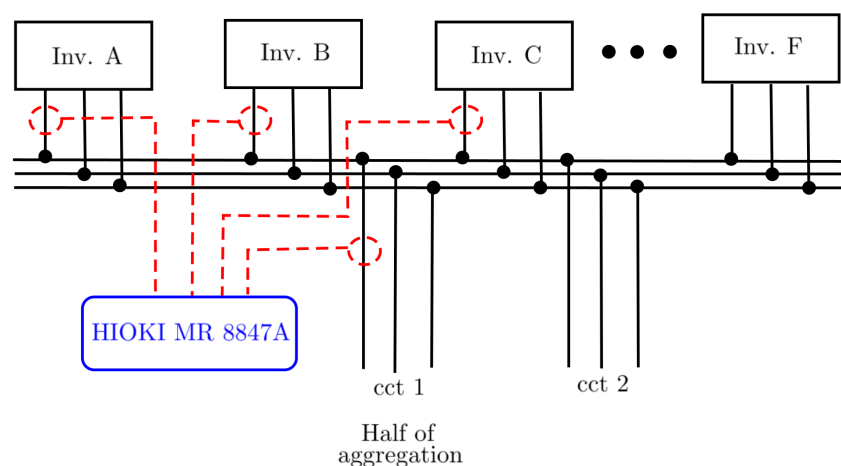


**Figure 7.** Measurement setup of solar PV system.

Measurements of output current were obtained while varying the number of inverters in operation. Maintaining an approximately equal power output from each inverter enables consideration of the harmonic emission characteristics compared to the number of inverters. Assuming a balanced system, the power output of each inverter was approximately 16 kW, or 80% of its rated value.

For Inverter A, the variation in harmonics in the 0–5 kHz range when compared against the number of inverters in operation is shown in Figure 8. It can be seen that the maximum individual harmonic magnitude in the high-frequency range is similar in magnitude to the 11th harmonic order in the low-frequency range when a single inverter is in operation. As the number of inverters increases, the magnitude of the harmonics in the 2–5 kHz range begins to decrease. The harmonic variation shows that, with only one inverter in operation, the magnitudes of the current harmonics in the 2–5 kHz range are similar to the magnitudes of the low-frequency harmonics. The maximum individual harmonic current component of 2.2% of the fundamental occurs at 4.2 kHz for single-inverter operation. It is evident that the harmonic content above 2 kHz can be as significant as that for low-frequency harmonics.

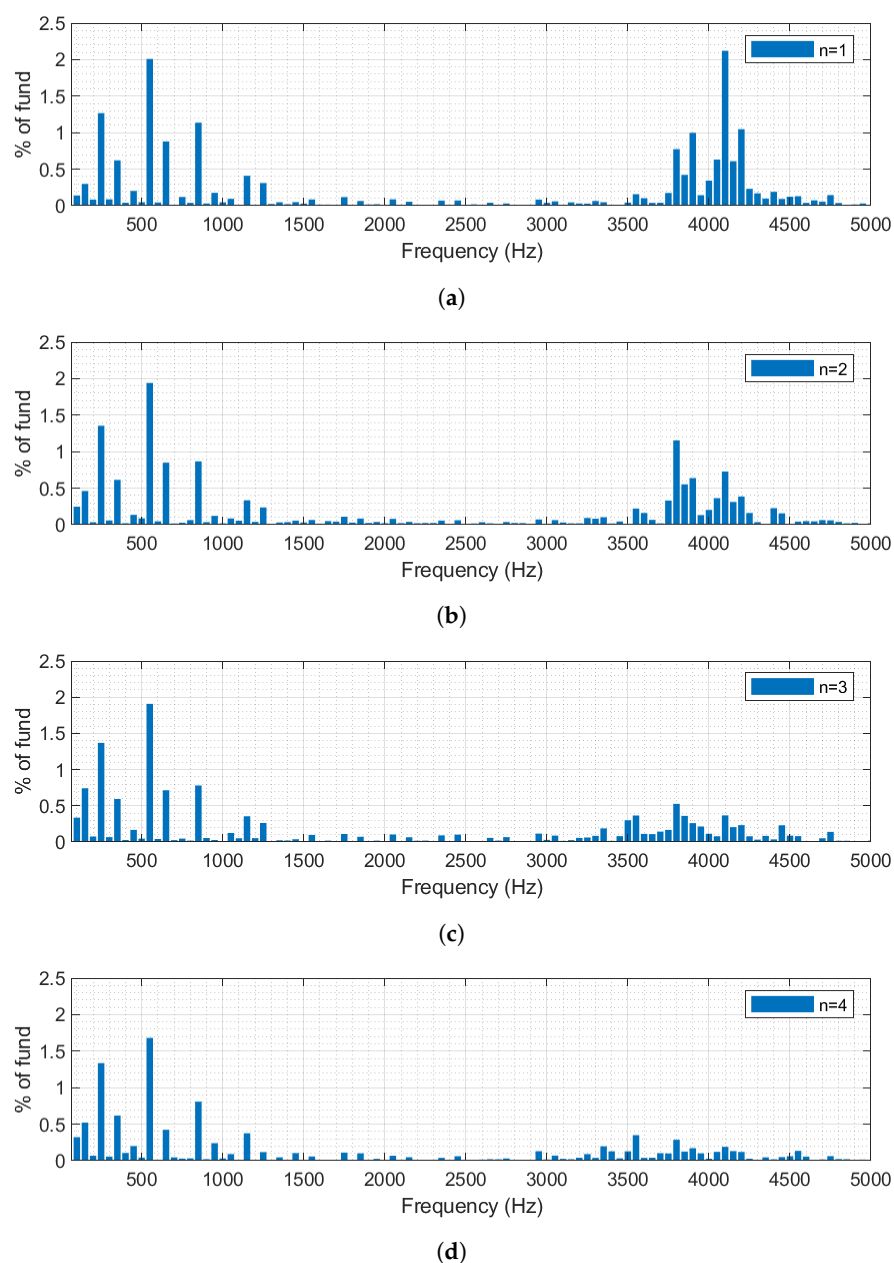


**Figure 8.** Inverter A harmonic spectrum up to 5 kHz (a)  $n = 1$  (b)  $n = 2$  (c)  $n = 3$  (d)  $n = 4$ .

The harmonic emissions concentrated within the 3–5 kHz can be identified as the resonance phenomena, in which peak magnitudes are decreased with the number of inverters.

## 5. Selection of Filter Components to Obtain Resonance at a Specific Frequency

The selection of filter components can have a large variation and depends on various factors such as the ripple attenuation at the switching frequency, the maximum ripple current allowance and the reactive power support by capacitors as shown in Figure 9. The resonant frequency variation is calculated based on the system parameters given in Table 2. These factors directly reflect on the resonant frequency where *LCL* filter components can be selected to place the resonance to a given frequency. With the known system parameters, there can be many possibilities, which can be derived for filter components. However, if the resonant frequency can be identified based on the measurements, those possibilities can be narrowed down to approximate to actual values.

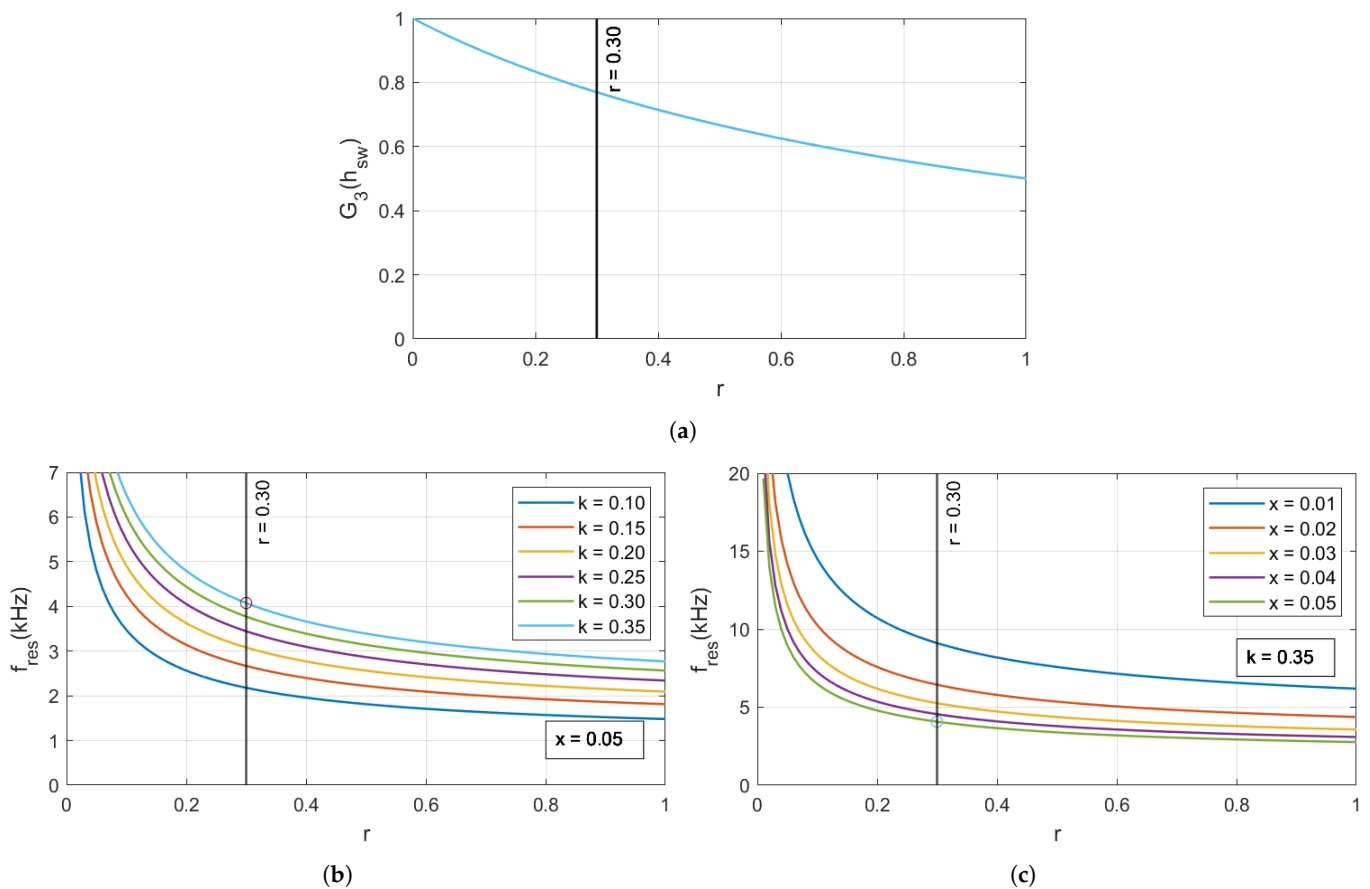


**Figure 9.** Variation of (a) ripple current attenuation at switching frequency; (b) resonant frequency keeping  $x = 0.05$ ; and (c) resonant frequency keeping  $k = 0.35$ , against index  $r$ .

Figure 9a illustrates the attenuation at switching frequency variation against the index  $r$ . The higher the grid-side inductance, the lower the switching frequency harmonic current portion that flows into the grid side. Additionally, the sizing of the inverter has to be compromised. Figure 9b provides details on how the resonant frequency changes with  $r$  for different allowed ripple current limits ( $k$ ) keeping the capacitor as a constant. Similarly, Figure 9c shows how the resonant frequency varies with  $r$  for different capacitor values keeping the inverter-side inductor as a constant. Assumed  $r$ ,  $k$  and  $x$  values given in Table 3 are marked as the black vertical line in Figure 9a, the red circle in Figure 9b and the blue circle in Figure 9c, respectively.

For modelling a generic PV inverter system in MATLAB/Simulink, it is important to decide on the probable filter type used by the inverter manufacturer and select appropriate

filter components based on the measurements. The three key assumptions of interest related to filter design should be: ripple current attenuation at switching frequency ( $r$ ); designed maximum allowed ripple current percentage ( $k$ ); and maximum reactive power absorption by the capacitor ( $x$ ). These parameters may be interdependent. For example, if we let  $r = 0.6$ , then there will be no possibility of selecting filter components to have a resonant frequency at 5 kHz complying with the filter design guide provided in Appendix A.

According to the system parameters given in Table 2, LCL filter component values were calculated such that the resonant frequency was 4.1 kHz. The value of 4.1 kHz is selected to be in line with the resonant frequency identified with the measurement setup in Section 4. Assumptions made to derive filter values are mentioned in Table 3. Considered LCL filter values to analyse the resonance impact in MATLAB/Simulink environment are given within brackets.

**Table 2.** System parameters.

Parameter	Symbol	Unit	Value
DC-link voltage	$V_{dc}$	V	600
Grid line voltage	$V_{LL}$	V	400
Grid nominal frequency	$f_n$	Hz	50
Nominal power	$P_r$	kW	20
Switching frequency	$f_{sw}$	kHz	15.8

**Table 3.** Calculated filter values.

Parameter	Symbol	Unit	Value
$L_2/L_1$ ratio	$r$		0.30
Maximum allowed ripple current	$k$	%	0.35
Maximum reactive power absorption	$x$	%	5
Minimum converter-side inductance	$L_{1,min}$	$\mu\text{H}$	290 (300)
Minimum grid-side inductance	$L_{2,min}$	$\mu\text{H}$	87 (100)
Grid inductance (assumed)	$L_g$	$\mu\text{H}$	50
Maximum filter capacitance	$C_f$	$\mu\text{F}$	20 (20)
resonant frequency	$f_{res}$	kHz	4.1

## 6. Simulation Results

A generic solar PV inverter system was modelled in the MATLAB/Simulink R2022b software environment to analyse resonance characteristics. A widely used control structure termed voltage-oriented control (VOC) is used to model the PV inverter using decoupled active and reactive current components in a synchronous reference frame (SRF). With the SRF three-phase AC currents and voltages are transformed into two DC components,  $d$ -axis and  $q$ -axis, making it easier to control the inverter current and voltage. The VOC-based controller guarantees fast transient response and high static performance via a current control loop [30] while maintaining a low harmonic content of the current fed to the grid. The typical PV inverter control structure is shown in Figure 10. The grid voltage and converter current are measured and fed into the  $dq$  controller, which generates a control signal that is used to control the inverter.

The MATLAB/Simulink model consists of four identical PV inverters and a simulation was made to capture the individual PV inverter current and the total grid current that is the aggregation of individual inverters. The filter values in Table 3 were applied and FFT analysis was performed on the current waveforms. The frequency spectrum is grouped into 200 Hz bands using the methodology detailed in informative Annex B of IEC 61000-4-7. The method specifies a measurement window of 200 ms independent of the nominal frequency [31].

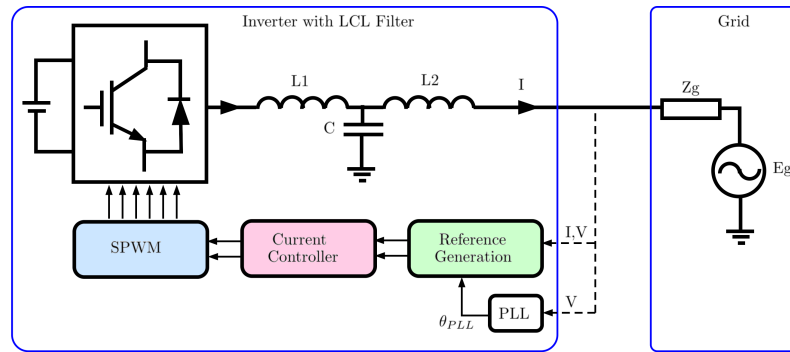


Figure 10. PV inverter control structure.

For each 200 Hz band, an amplitude at the middle of the frequency band was derived using Root Sum Square (RSS). Let  $Y_{Cf}$  is the amplitude of the spectrum at frequency  $f$ , and then the RSS value of band  $b$  ( $Y_{B,b}$ ) is given in (16). The same technique was used from 1 kHz to analyse the resonant frequency characteristics.

$$Y_{B,b} = \sqrt{\sum_{f=b-95 \text{ Hz}}^{f=b+100 \text{ Hz}} Y_{Cf}^2} \quad (16)$$

### 6.1. Resonance Introduced by LCL Filters

The frequency resonance obtained for an LCL filter system in Section 3 and the frequency spectrum of output currents in MATLAB/Simulink model are depicted in Figure 11. The grid impedance has been set as a constant and the number of inverters ( $n$ ) in operation is changed. The following outcomes are observed:

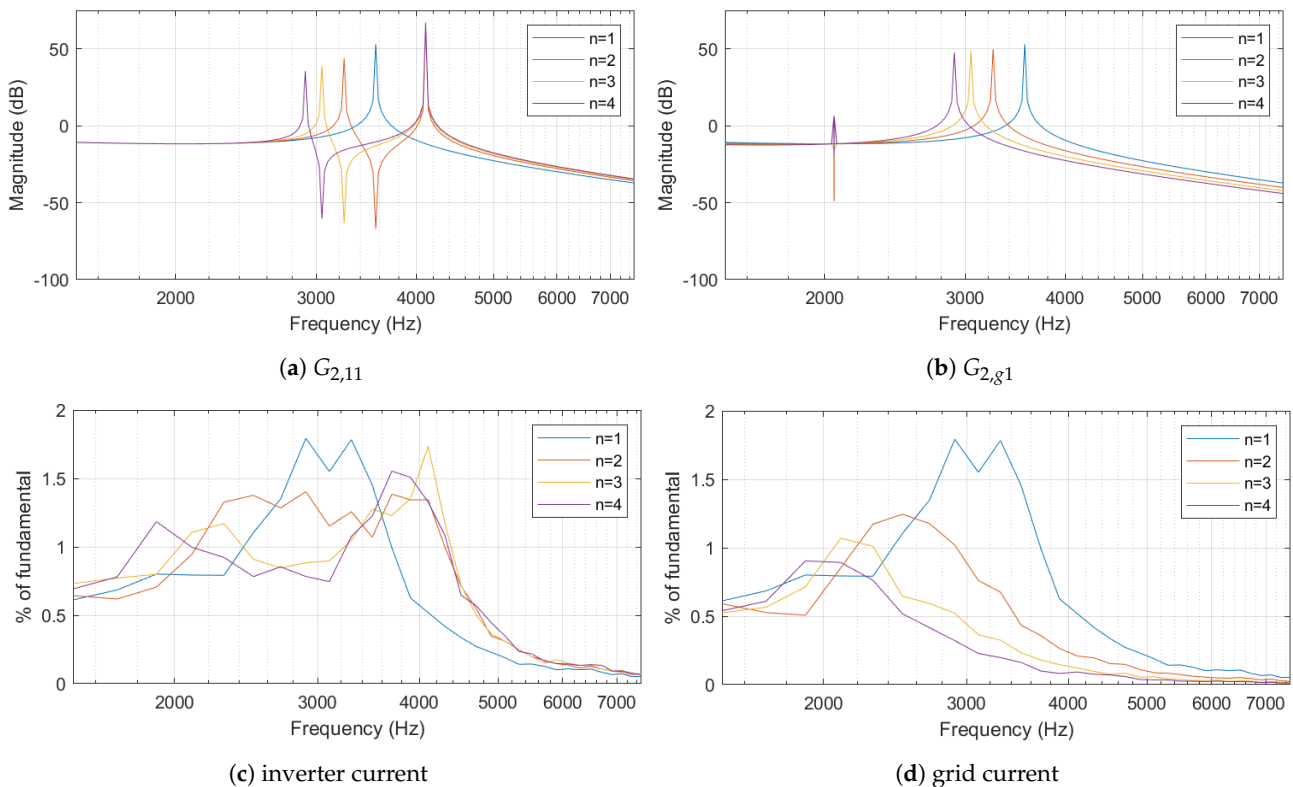
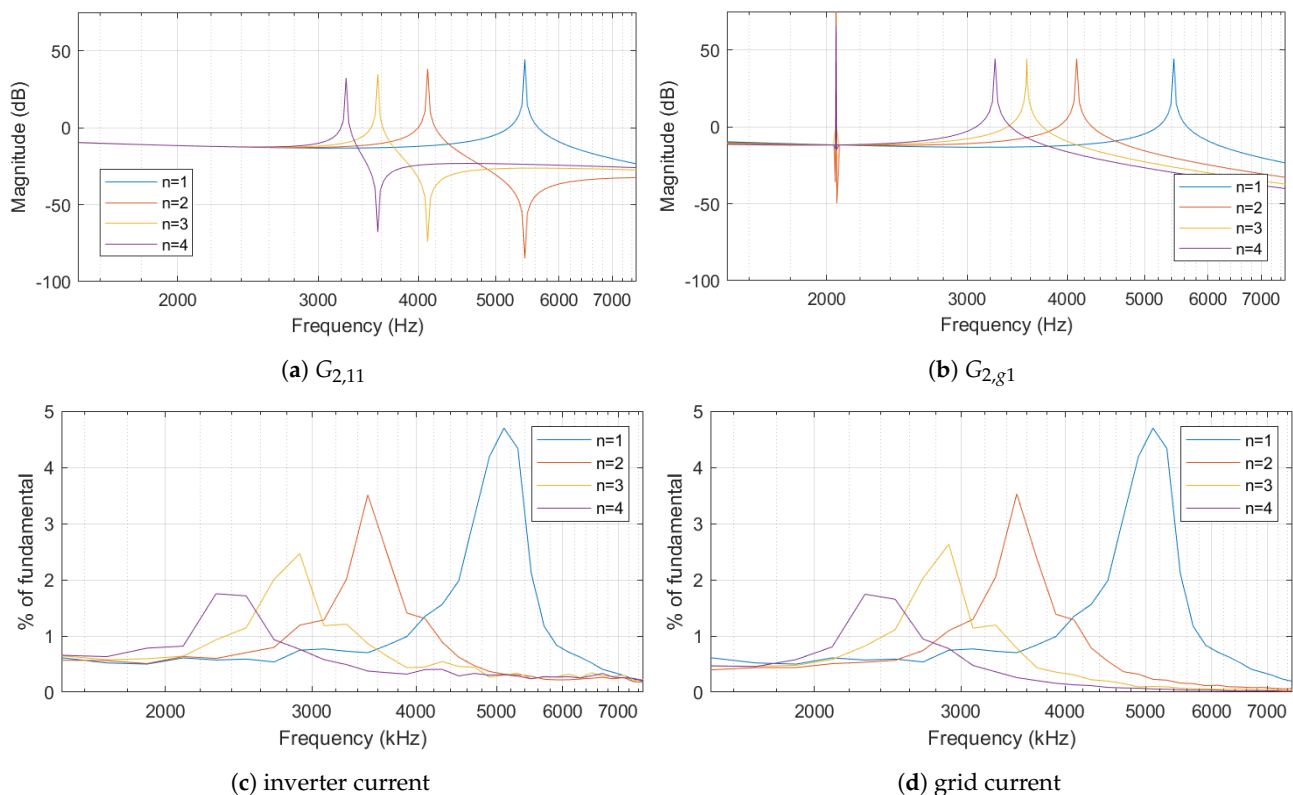


Figure 11. Resonant frequency characteristics of the LCL filter: (a)  $G_{2,11}$ ; (b)  $G_{2,g1}$ ; (c) grouped harmonic spectrum of inverter current; and (d) grouped harmonic spectrum of grid current.

- The harmonic spectrum of the individual inverter and grid current is not identical except where  $n = 1$ .
- Two distinct resonant points can be identified based on the forward self-admittance presented in Figure 11a, where  $n > 1$ . This is identified in the inverter current harmonic spectrum in Figure 11c, where  $f_{LCL}$  occurred at approximately 4.2 kHz.
- Due to the two resonant points in the inverter current frequency spectrum, it can be approximated as a broadband harmonic emission lying between  $f_{res,n}$  and  $f_{LCL}$ .
- The resonant point due to multiple inverters ( $f_{res,n}$ ) shifts toward lower frequencies as  $n$  increases.
- The inverter current harmonic spectrum provides a broadband resonance spectrum, which is due to the two resonant peaks. On the contrary, the narrowband resonance spectrum is seen in the grid current harmonic spectrum due to the single resonant peak.

### 6.2. Resonance Introduced by LC Filters

The resonance phenomenon created by an LC filter in Section 3 is compared with the MATLAB/Simulink model in Figure 12 with the grid impedance kept constant. The number of inverters ( $n$ ) in operation is changed. The following outcomes are observed:



**Figure 12.** Resonant frequency characteristics of LC filter: (a)  $G_{2,11}$ ; (b)  $G_{2,g1}$ ; (c) grouped harmonic spectrum of inverter current; and (d) grouped harmonic spectrum of grid current.

- The harmonic spectrum of individual inverters and grid current is identical to each other at all times.
- A single resonant point can be identified based on the forward self-admittance presented in Figure 12a as well as in the  $G_{g,1}$  presented in Figure 12b.
- The resonant point due to  $n$  inverters ( $f_{res,n}$ ) shifts toward lower frequencies as  $n$  increases.
- Both inverter current and grid current harmonic spectra provide a narrowband resonance spectrum due to their single resonant peak.

### 6.3. Impact of Grid Impedance on Resonance

The impact of grid impedance on the resonant frequency is plotted in Figure 13. The number of inverters in operation has been set to three ( $n = 3$ ). The results show that the resonant frequency shifts towards a lower frequency range as the grid impedance increases. Whether it is a weak or strong grid, resonance shifts towards the lower frequency range when the number of inverters increases. However, this resonance shift can be further shifted downwards for a weaker grid. Thus, the grid stiffness has to be considered when multiple inverters are connected as it may interfere with the lower frequency harmonics.

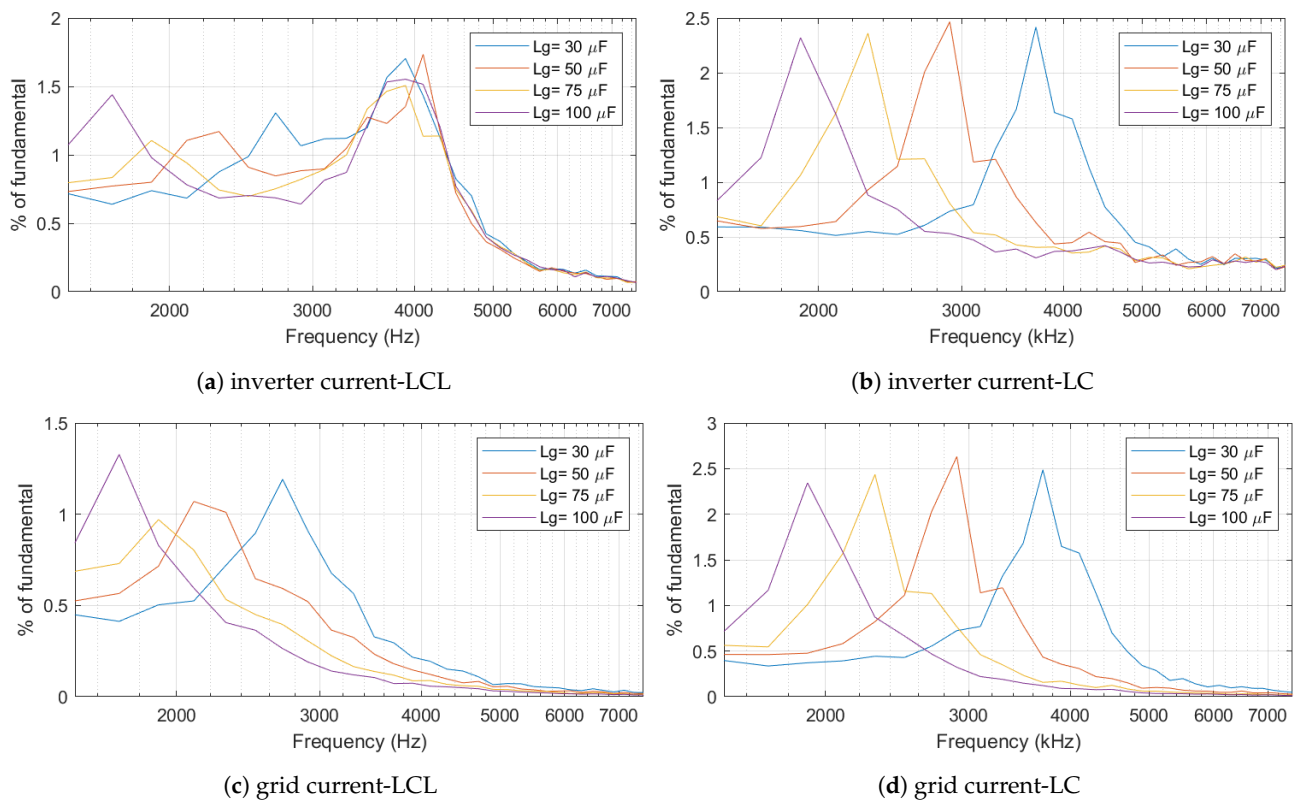


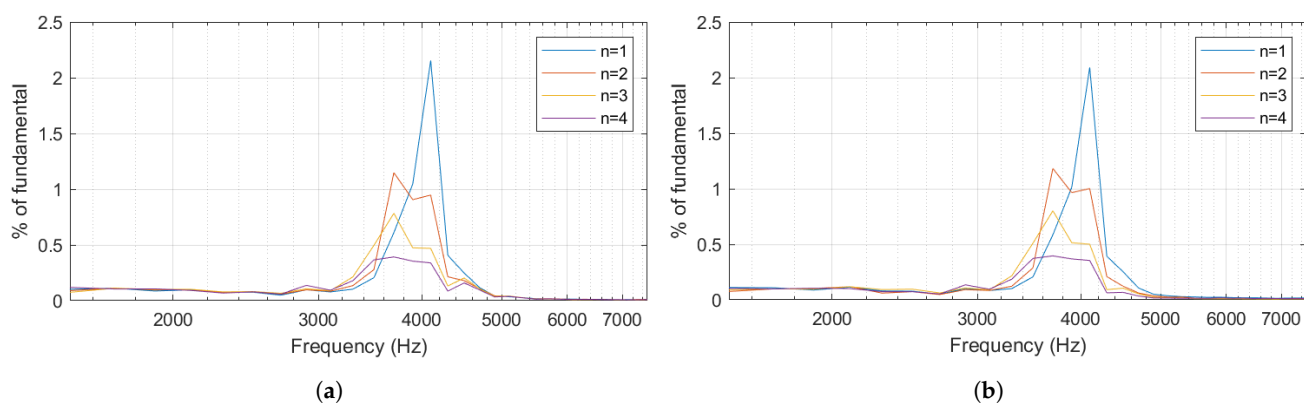
**Figure 13.** Resonant frequency characteristics variation against grid impedance: (a) inverter current with LCL filter; (b) grid current with LCL filter; (c) inverter current with LC filter; and (d) grid current with LC filter.

## 7. Discussion

This section discusses the aspects of deciding the filter type used in the PV inverters in Section 4. It was observed that the individual inverter current and the aggregated current have similar (for LC filters) and different (for LCL filters) characteristics. Measuring both currents and analysing the harmonic spectra was helpful in identifying the type of filter used in the PV inverter.

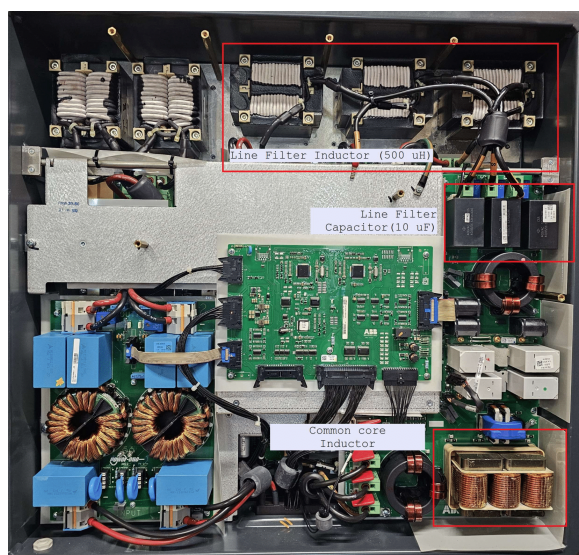
### 7.1. Filter Type Identification Based on Measurements

Figure 14 shows the harmonic spectrum between 1.5 kHz and 7.5 kHz for Inverter A and the aggregation cable where  $n$  represents the number of inverters in operation. Similar resonance characteristics irrespective of the number of inverters in operation indicate that the PV inverter does not have an LCL filter.



**Figure 14.** Resonant frequency spectrum: (a) inverter A current (b) aggregation cable current.

However, it was identified that commercial PV inverters have a common core inductor placed between the line filter and the grid to reduce the high-frequency noise emitting from external sources and within the inverter itself. Figure 15 is a photograph of the internal components of one of the inverters monitored in this study.



**Figure 15.** Photograph of three-phase solar PV inverter with identified filter components.

### 7.2. Comparison of Field Measurements with Developed Model

The modelling of the common core reactor is challenging as both mutual and self-inductance need to be considered while verifying the model with the measurements. In differential mode, the resultant magnetic field created by all three phases could be very low, thus the parasitic capacitance impact must also be considered for accurate modelling. For a common-mode winding, the resultant magnetic field created by all three phases is relatively high and the parasitic capacitance impact can be neglected. In this study, it was modelled as a common-mode reactor in MATLAB/Simulink platform, where parasitic capacitors were neglected.

The measurement results and the MATLAB/Simulink model results are depicted in Figure 16. By measuring the filter components of a PV inverter those values were incorporated into the MATLAB/Simulink model to verify the model accuracy. Filter components were selected as  $L_1 = 500 \mu\text{H}$  and  $C_f = 10 \mu\text{F}$ , which satisfies the values derived for  $L_{1,min}$  and  $C_{f,max}$ .

If only an LC filter was present, the current harmonic spectrum should be somewhat similar to Figure 16c,d. The resonance peak shift is substantially high. However, adding a

mutual inductance block in MATLAB/Simulink to represent the common-core inductance provides quite similar characteristics seen in measurements. The resonance shift becomes much less compared to that of the  $LC$  filter. According to Figure 16e, there is an additional resonance point that can be identified, which is due to the self-inductance of the common-core choke. However, the impact of parasitic capacitance on this resonance has to be studied to fully understand its behaviour.

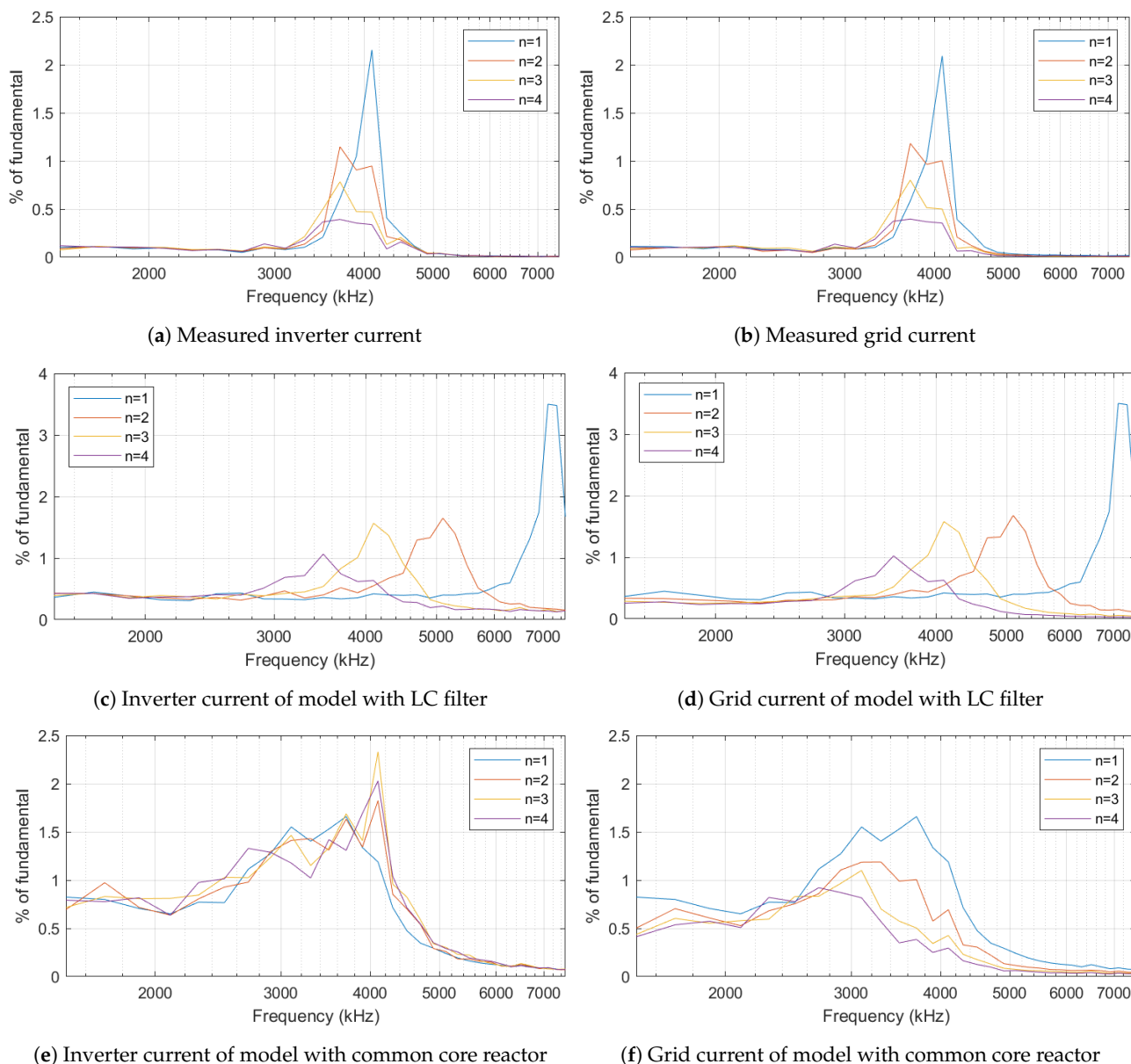


**Figure 16.** Measurement and modelling results: (a) measured inverter current; (b) measured grid current; (c) inverter current with MATLAB model considering  $LC$  only; (d) grid current with MATLAB model considering  $LC$  only; (e) inverter current with MATLAB model considering  $LC$  and common core reactor; and (f) grid current with MATLAB model considering  $LC$  and common core reactor.

### 7.3. Future Works

The understanding of resonance is helpful in developing a generic solar PV model for high-frequency harmonic analysis. However, this study only considered resonant frequency and the most common  $LCL$  and  $LC$  filter types. There could be many combinations of filter components to align with a specific frequency. The advanced control techniques and

different filter types (in addition to conventional filters) used in inverter manufacturers have to be identified to develop an accurate model for high-frequency analysis.

## 8. Conclusions

All solar PV inverters consist of a front-end filter to reduce the supraharmmonic emissions introduced by its PWM technique. However, accurate high-frequency harmonic modelling requires knowing the filter type as well as the filter component values, which are only available to inverter manufacturers. This paper presents the solar PV inverter modelling aspects considering the resonance impact.

1. By measuring the current flowing in both the inverter terminals and the aggregation cable, it is possible to determine the resonant frequency. This process involves connecting the inverters one at a time and then analyzing the frequency spectra to identify the dampening of the resonance peak.
2. The similarity between two frequency spectra can be used to identify the type of filter used inside the PV inverter. For *LC* filters, both frequency spectra have the same characteristics—one resonant frequency. For *LCL* filters, both spectra are not identical as the inverter current spectrum contains an additional resonant peak introduced due to the *LCL* filter components themselves.
3. Based on the resonant frequency and the filter type, filter the components that are to be selected.  $n = 1$  scenario selection is appropriate as  $n$  increases the system becomes more complex to derive the components.
4. Common core choke id to be considered for fine tuning of the model to replicate the frequency spectrum obtained from measurements.

Model accuracy depends on several factors, i.e., control technology, active filtering technique, parasitic components, damping resistors, passive filtering techniques, secondary emissions, neighbouring power electronic devices, etc. Thus, high-frequency modelling is a challenging task.

This paper provides a mathematical approach to understanding the resonant frequency variation within a system as the number of inverters changes. The characteristics were verified with the MATLAB/Simulink inverter model for both *LCL* and *LC* filter types. The model was subsequently updated to incorporate a common core inductor-based filter and results were compared with field measurements.

**Author Contributions:** Conceptualization, K.P.; methodology, K.P., S.E. and J.D.; original draft preparation, K.P.; review and editing, S.E., J.D. and D.R. All authors have read and agreed to the published version of the manuscript.

**Funding:** This research received external funding from the Australian Government via the Global Innovations Linkage (GIL) program grant number: GIL73697.

**Data Availability Statement:** Data are contained within the article.

**Conflicts of Interest:** The authors declare no conflicts of interest.

## Appendix A. LCL Filter Design Procedure

1. Design the converter-side inductance ( $L_1$ ) selecting the required current ripple on the converter side according to (A1), where  $\Delta i_{L1,max}$ ,  $i_{r,pk}$ ,  $V_{DC}$  and  $f_{sw}$  are the maximum allowed current ripple, rated peak current, DC bus voltage and switching frequency, respectively.

$$L_{1,min} = \frac{V_{DC}}{8 \cdot f_{sw} \Delta i_{L1,max}} \quad (A1)$$

$$\Delta i_{L1,max} = k \cdot i_{r,pk}$$

- Design the grid-side inductance ( $L_2$ ), which can either be the converter-side inductance alone or with a combination, which includes the grid inductance. Attention is drawn to the fact that, the resonant frequency of the system is determined by considering grid impedance. Assuming (1) is true, the outer inductance is calculated as a function of  $L_1$ , using the index  $r$  which is the relation between two inductances as follows.

$$L_2 = r \cdot L_1 \quad (\text{A2})$$

- Determine the value of filter capacitor  $C_f$  based on the amount of reactive power absorption at rated conditions by the inverter as follows,

$$C_b = \frac{P_{rated}}{2\pi f_n V_{LL}^2} \quad (\text{A3})$$

$$C_{f,max} = x \cdot C_b$$

where  $C_b$ ,  $P_r$ ,  $V_{LL}$  and  $x$  are the base capacitance, rated power of the inverter, line-line voltage and the reactive power absorption as a percentage, i.e., for 5% absorption,  $x = 0.05$ .

- Determine the required current ripple reduction at switching frequency to select a suitable value for index  $r$ . At switching frequency, transfer functions given in (7) can be re-written as:

$$G_2(h_{sw}) = \frac{i_2(h_{sw})}{v_i(h_{sw})} = \frac{z_{LC}^2}{\omega_{sw} L_1 \cdot |\omega_{res}^2 - \omega_{sw}^2|}$$

$$G_1(h_{sw}) = \frac{i_1(h_{sw})}{v_i(h_{sw})} \approx \frac{1}{\omega_{sw} L_1} \quad (\text{A4})$$

$$G_3(h_{sw}) = \frac{i_2(h_{sw})}{i_i(h_{sw})} \approx \frac{z_{LC}^2}{|\omega_{res}^2 - \omega_{sw}^2|}$$

where  $h_{sw}$  is the order of switching frequency harmonic and  $z_{LC}^2 = (L_2 C_f)^{-1}$ . By applying (A2) and (A3), the above expression for  $G_3$  can be written as follows, where  $a = L_1 C_b \omega_{sw}^2$  (which is a constant).

$$G_3(h_{sw}) = \frac{i_2(h_{sw})}{i_i(h_{sw})} = \frac{1}{|1 + r(1 - a \cdot x)|} \quad (\text{A5})$$

- Verify the resonant frequency satisfying the limits in (A8) which can be re-written as follows, where  $b = L_1 C_b$ .

$$f_{res} = \frac{1}{2\pi} \sqrt{\frac{1+r}{b \cdot x \cdot r}} \quad (\text{A6})$$

- Set the damping to the resonance peak by adding a resistor in series with the filter capacitor ( $C_f$ ). Damping resistor value can be determined as follows.

$$R_d = \frac{1}{3C_f} \sqrt{\frac{L_1 L_2 C_f}{L_1 + L_2}} \quad (\text{A7})$$

- Maintain resonant frequency ( $f_{res}$ ) at a value between the half of the switching frequency ( $f_{sw}$ ) and ten times that of the nominal frequency ( $f_n$ ) for the safe operation of inverter in order to attenuate switching frequency harmonics and to avoid interference with low-frequency harmonics disturbances.

$$10 \cdot f_n < f_{res} < \frac{f_{sw}}{2} \quad (\text{A8})$$

8. The voltage drop across the filter inductors ( $L_1 + L_2$ ) should be maintained below 10% of its rated value to ensure reliable voltage supply at the inverter terminals, otherwise a higher DC-link voltage will be required [6,32].

$$Z_{L1} + Z_{L2} < 0.1 \times Z_b \quad (\text{A9})$$

## Appendix B. Two-Inverter System

Figure A1 illustrates the general arrangement of two inverters with LCL filters, which are connected in parallel, each inverter is represented by its Thévenin equivalent.

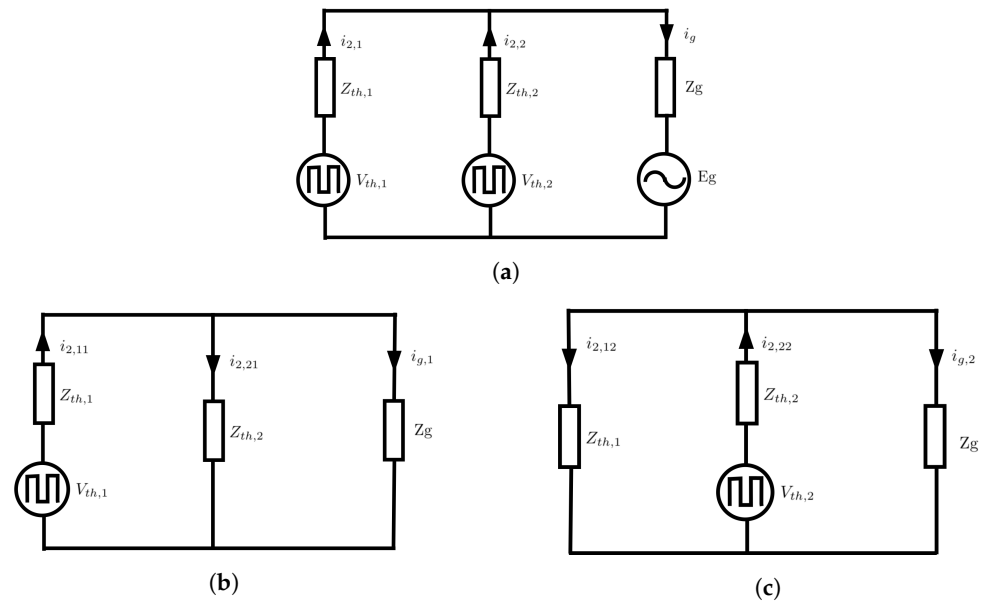


**Figure A1.** Superposition theorem for two inverters in parallel: (a) general arrangement; (b) Inverter 1 only; and (c) Inverter 2 only.

For a two-inverter system, the forward-trans admittance matrix can be written as follows:

$$i_2 = G_2 \times V_i$$

$$\begin{bmatrix} i_{2,1} \\ i_{2,2} \end{bmatrix} = \begin{bmatrix} G_{2,11} & G_{2,12} \\ G_{2,21} & G_{2,22} \end{bmatrix} \times \begin{bmatrix} V_{i,1} \\ V_{i,2} \end{bmatrix} \quad (\text{A10})$$

where  $G_{2,xy}$  represent the forward-trans admittance seen by inverter  $x$  due to the inverter  $y$ . The diagonal elements of  $G_2$  matrix have identical values and off-diagonal elements have negative identical values. Each element of  $G_2$  matrix can be determined by applying the superposition theorem to the system as shown in Figure A1b,c.

When the second inverter connects, the grid impedance seen by Inverter 1 is altered. This can be represented by  $Z_M$  calculated as the resultant of two parallel impedances, i.e., grid impedance and Inverter 2 filter Thévenin impedance, assuming that the second inverter voltage is zero. Likewise, multiple inverter system can be represented by the single-inverter model where grid impedance ( $Z_g$ ) is replaced by  $Z_M$  as follows:

$$Z_M = Z_{th} // Z_g$$

$$Z_M = \left[ \frac{Z_{th} Z_g}{Z_{th} + Z_g} \right] \quad (\text{A11})$$

The transfer function between  $i_{2,11}$  and  $V_{i,1}$  is given by (A12).

$$G_{2,11} = \frac{i_{2,11}}{V_{i,1}} = \frac{Z_c}{Z_1(Z_2 + Z_M) + Z_c(Z_2 + Z_M) + Z_1 Z_c} \quad (\text{A12})$$

$$G_{2,11} = \frac{k_{th}}{Z_{th} + Z_M}$$

The coupling effect on the Inverter 1 current ( $i_{2,12}$ ), experienced by the Inverter 2 voltage is given by (A13).

$$i_{2,12} = \frac{Z_g}{Z_g + Z_{th}} \cdot i_{2,11} \quad (\text{A13})$$

The transfer function between  $i_{2,12}$  and  $V_{i,2}$  is given by (A14).

$$G_{2,12} = \frac{i_{2,12}}{V_{i,2}} = \frac{Z_g}{Z_g + Z_{th}} \cdot G_{2,11} \quad (\text{A14})$$

$$G_{2,12} = \left[ \frac{Z_g}{Z_g + Z_{th}} \right] \cdot \left[ \frac{k_{th}}{Z_{th} + Z_M} \right]$$

Similarly, the transfer function between grid current component of Inverter 1 ( $i_{g,1}$ ) and Inverter 1 voltage ( $V_{i,1}$ ) is given by (A15). This is useful to characterise the grid current component caused by each inverter.

$$G_{2,g1} = \frac{i_{g,1}}{V_{i,1}} = G_{2,11} - G_{2,12} \quad (\text{A15})$$

## References

- Zhu, T.; Huang, G.; Ouyang, X.; Zhang, W.; Wang, Y.; Ye, X.; Wang, Y.; Gao, S. Analysis and Suppression of Harmonic Resonance in Photovoltaic Grid-Connected Systems. *Energies* **2024**, *17*, 1218. [\[CrossRef\]](#)
- Subhani, S.; Cuk, V.; Cobben, J. A literature survey on power quality disturbances in the frequency range of 2–150 kHz. *Renew. Energy Power Qual. J.* **2017**, *1*, 405–410. [\[CrossRef\]](#)
- Gao, J.; Zhao, Y.; Lu, Y.; Gao, Y.; Zhang, X. Exploration of Factors Affecting Resonance in Photovoltaic Cluster Grid Integration System. *J. Phys. Conf. Ser.* **2024**, *2890*, 012017. [\[CrossRef\]](#)
- Liu, Q.; Liu, F.; Zou, R.; Li, Y. Harmonic Resonance Characteristic of Large-Scale PV Plant: Modelling, Analysis, and Engineering Case. *IEEE Trans. Power Deliv.* **2022**, *37*, 2359–2368. [\[CrossRef\]](#)
- Kaufhold, E.; Meyer, J.; Schegner, P. Impact of grid impedance and their resonance on the stability of single-phase PV-inverters in low voltage grids. In Proceedings of the 2020 IEEE 29th International Symposium on Industrial Electronics (ISIE), Delft, The Netherlands, 17–19 June 2020; pp. 880–885. [\[CrossRef\]](#)
- Liserre, M.; Blaabjerg, F.; Hansen, S. Design and control of an LCL-filter-based three-phase active rectifier. *IEEE Trans. Ind. Appl.* **2005**, *41*, 1281–1291. [\[CrossRef\]](#)
- Liserre, M.; Blaabjerg, F.; Hansen, S. Design and control of an LCL-filter based three-phase active rectifier. In Proceedings of the Conference Record of the 2001 IEEE Industry Applications Conference. 36th IAS Annual Meeting (Cat. No.01CH37248), Chicago, IL, USA, 30 September–4 October 2001; Volume 1, pp. 299–307. [\[CrossRef\]](#)
- Lee, J.Y.; Cho, Y.P.; Kim, H.S.; Jung, J.H. Design Methodology of Passive Damped LCL Filter Using Current Controller for Grid-Connected Three-Phase Voltage-Source Inverters. *J. Power Electron.* **2018**, *18*, 1178–1189. [\[CrossRef\]](#)
- Moreno-Munoz, A.; Gil-de Castro, A.; Romero-Cavada, E.; Rönnberg, S.; Bollen, M. Supraharmonics (2 to 150 kHz) and multi-level converters. In Proceedings of the 2015 IEEE 5th International Conference on Power Engineering, Energy and Electrical Drives (POWERENG), Riga, Latvia, 1–13 May 2015; pp. 37–41. [\[CrossRef\]](#)
- Ruan, X.; Wang, X.; Pan, D.; Yang, D.; Li, W.; Bao, C. (Eds.) Design of LCL Filter. In *Control Techniques for LCL-Type Grid-Connected Inverters*; CPSS Power Electronics Series; Springer: Singapore, 2018; pp. 31–61. [\[CrossRef\]](#)
- Gharani Khajeh, K.; Solatalkaran, D.; Zare, F.; Mithulananthan, N. An enhanced full-feedforward strategy to mitigate output current harmonics in grid-tied inverters. *IET Gener. Transm. Distrib.* **2021**, *15*, 827–835. [\[CrossRef\]](#)
- Wang, Q.; Ju, B.; Zhang, Y.; Zhou, D.; Wang, N.; Wu, G. Design and implementation of an LCL grid-connected inverter based on capacitive current fractional proportional—Integral feedback strategy. *IET Control Theory Appl.* **2020**, *14*, 2889–2898. [\[CrossRef\]](#)
- Adamas-Pérez, H.; Ponce-Silva, M.; Mina-Antonio, J.D.; Claudio-Sánchez, A.; Rodríguez-Benítez, O.; Rodríguez-Benítez, O.M. A New LCL Filter Design Method for Single-Phase Photovoltaic Systems Connected to the Grid via Micro-Inverters. *Technologies* **2024**, *12*, 89. [\[CrossRef\]](#)

14. Sgrò, D.; Souza, S.A.; Tofoli, F.L.; Leão, R.P.S.; Sombra, A.K.R. An integrated design approach of LCL filters based on nonlinear inductors for grid-connected inverter applications. *Electr. Power Syst. Res.* **2020**, *186*, 106389. [[CrossRef](#)]
15. Val Escudero, M.; Lietz, G.; Emin, Z.; Jensen, C.; Kocewiak, Ł. *CIGRE TB 766: JWG C4/B4.38 Network Modelling for Harmonic Studies*; CIGRE: Paris, France, 2019.
16. Ramirez, A. Frequency Domain Modeling of Photovoltaic Systems for Transient Analysis. *IEEE Trans. Power Deliv.* **2022**, *37*, 3762–3770. [[CrossRef](#)]
17. Darmawardana, D.; Perera, S.; Robinson, D.; Meyer, J.; Jayatunga, U. Important Considerations in Development of PV Inverter Models for High Frequency Emission (Supraharmonic) Studies. In Proceedings of the 2020 19th International Conference on Harmonics and Quality of Power (ICHQP), Dubai, United Arab Emirates, 6–7 July 2020; pp. 1–6. [[CrossRef](#)]
18. Espín-Delgado, A.; Rönnberg, S.; Busatto, T.; Ravindran, V.; Bollen, M. Summation law for supraharmonic currents (2–150 kHz) in low-voltage installations. *Electr. Power Syst. Res.* **2020**, *184*, 106325. [[CrossRef](#)]
19. Akhavan, A.; Mohammadi, H.R.; Guerrero, J.M. A comprehensive control system for multi-parallel grid-connected inverters with LCL filter in weak grid condition. *Electr. Power Syst. Res.* **2018**, *163*, 288–300. [[CrossRef](#)]
20. Sarajian, S. LCL filter Design and Current Control of Grid Interfaced Voltage Source Inverter. *Int. J. Electron. Commun. Electr. Eng.* **2014**, *4*, 26–40.
21. Liserre, M.; Blaabjerg, F.; Dell’Aquila, A. Step-by-step design procedure for a grid-connected three-phase PWM voltage source converter. *Int. J. Electron.* **2004**, *91*, 445–460. [[CrossRef](#)]
22. Ranjan, A.; Giribabu, D. Design of LCL Filter For Grid Connected Three Phase Three Level Inverter to Meet IEEE 519 Standards. In Proceedings of the 2023 IEEE International Students’ Conference on Electrical, Electronics and Computer Science (SCEECS), Bhopal, India, 18–19 February 2023; pp. 1–6. [[CrossRef](#)]
23. Hasan, S.; Suherman; Saragi, D.P.; Siregar, Y.; Al-Akaidi, M. The LCL filter design for three phase DC-AC voltage converter. *J. Phys. Conf. Ser.* **2021**, *1783*, 012067. [[CrossRef](#)]
24. Dursun, M.; Döşoğlu, M.K. LCL Filter Design for Grid Connected Three-Phase Inverter. In Proceedings of the 2018 2nd International Symposium on Multidisciplinary Studies and Innovative Technologies (ISMSIT), Ankara, Turkey, 19–21 October 2018; pp. 1–4. [[CrossRef](#)]
25. Saha, T.; Mitra, A.; Halder, B. Design of LCL Filter for SPWM Inverter Based on Switching Frequency and THD Criterion. In *Electronic Systems and Intelligent Computing*; Springer: Singapore, 2020; pp. 439–451. [[CrossRef](#)]
26. Jayathilaka, I.; Lakpriya, L.; De Alwis, D.; Jayakody, G.; Hemapala, K.; Karunadasa, J.; Lakshika, H. DQ Transform Based Current Controller for Single-Phase Grid Connected Inverter. In Proceedings of the 2018 2nd International Conference on Electrical Engineering (EECon), Colombo, Sri Lanka, 28–28 September 2018; pp. 32–37. [[CrossRef](#)]
27. Said-Romdhane, M.B.; Naouar, M.W.; Belkhdja, I.S.; Monmasson, E. An Improved LCL Filter Design in Order to Ensure Stability without Damping and Despite Large Grid Impedance Variations. *Energies* **2017**, *10*, 336. [[CrossRef](#)]
28. Juntunen, R.; Korhonen, J.; Musikka, T.; Smirnova, L.; Pyrhönen, O.; Silventoinen, P. Comparative analysis of LCL-filter designs for paralleled inverters. In Proceedings of the 2015 IEEE Energy Conversion Congress and Exposition (ECCE), Montreal, QC, Canada, 20–24 September 2015; pp. 2664–2672. [[CrossRef](#)]
29. Lu, M.; Wang, X.; Blaabjerg, F.; Loh, P.C. An analysis method for harmonic resonance and stability of multi-paralleled LCL-filtered inverters. In Proceedings of the 2015 IEEE 6th International Symposium on Power Electronics for Distributed Generation Systems (PEDG), Aachen, Germany, 22–25 June 2015; pp. 1–6. [[CrossRef](#)]
30. Zhao, T.; Zong, Q.; Zhang, T.; Xu, Y. Study of photovoltaic three-phase grid-connected inverter based on the grid voltage-oriented control. In Proceedings of the 2016 IEEE 11th Conference on Industrial Electronics and Applications (ICIEA), Hefei, China, 5–7 June 2016; pp. 2055–2060. [[CrossRef](#)]
31. Grevener, A.; Meyer, J.; Rönnberg, S.; Bollen, M.; Myrzik, J. Survey of supraharmonic emission of household appliances. *CIREN—Open Access Proc. J.* **2017**, *2017*, 870–874. [[CrossRef](#)]
32. Hojabri, M. Design, application and comparison of passive filters for three-phase grid-connected renewable energy systems. *ARPJ. Eng. Appl. Sci.* **2015**, *10*, 10691–10697.

**Disclaimer/Publisher’s Note:** The statements, opinions and data contained in all publications are solely those of the individual author(s) and contributor(s) and not of MDPI and/or the editor(s). MDPI and/or the editor(s) disclaim responsibility for any injury to people or property resulting from any ideas, methods, instructions or products referred to in the content.